ME670A
ADDITIVE MANUFACTURING
Term paper 2024-25 1st Sem

Manipulating melt pool thermofluidic transport in directed energy deposition driven by a laser intensity spatial shaping strategy

Guided by : Dr. Arvind Kumar

Name : Rajit Tiwari
210818

ABSTRACT

LIST OF FIGURES AND TABLES

1. INTRODUCTION 5-6

1.1 Additive Manufacturing

1.1.1 Benefits of Additive Manufacturing

1.2 Direct energy deposition process

2. PROBLEM DEFINITION 6-7

2.1 Model Configurations

3. METHODOLOGY 7-10

3.1. Basic assumptions

3.2. Governing equation

3.3. Boundary conditions

3.4. Material Properties

4. EXPERIMENTAL ANALYSIS 10

4.1 Numerical Simulation

5. RESULTS AND DISCUSSION 10-14

5.1. Experiment Results

5.2. Simulation Results

5.3. Velocity Distribution

6. CONCLUSIONS 14

7. SCOPE FOR FUTURE WORK 14

8. REFERENCES 15

ABSTRACT

In this paper, a three-dimensional thermofluidic coupling transport model has been developed to identify the melt pool formation and solidification in Direct Energy Deposition (DED) Process. Lasers are used as the energy source with different special laser intensity profiles (SLIPs), including circular super-Gaussian profile (C-SGP), longitudinal elliptical Gaussian profile (LE-GP) and transverse elliptical Gaussian profile (TE-GP). Main aim is to determine effect of different SLIPs on shape and size of the melt pool. Temperature profile, velocity profile and shape of the melt pool has been studied for different SLIPs. The results show that the SLIPs significantly determine the melt pool geometries, fluid flow dynamics and temperature gradient within the melt pool. The Marangoni effect is shown in all three SLIPs with strongest in LE-GP and weakest in TE-GP. The heat transport of the melt pool under the C-SGP and TE-GP strategies are jointly dominated by convective and conductive heat transfer, while those under the LE-GP strategy are dominated by convective heat transfer.

LIST OF FIGURES

Fig.1. Schematic of L-DED with multichannel coaxial powder feeding

Fig.2. Schematic of the simulated physical model and its computational mesh.

Fig.3. (a) Circular super gaussian profile for k = 4.2. (b) Elliptic Gaussian intensity profile.

Fig.4. Cross-sectional profiles of the melt pool under the C-SGP with different laser powers: (a) 600 W, (b) 700 W, and (c) 800 W.

Fig.5. Measured and predicted melt pool sizes: (a) height; (b) width; (c) penetration depth.

Fig.6. Schematics of melt pool geometries under three SLIPs: (a) C-SGP, (b) TE-GP, and (c) LE-GP.

Fig.7. Temperature fields under the three SLIPs.

Fig.8. Velocity fields of the melt pool under three SLIPs: (a) C-SGP, (b) TE-GP, and (c) LE-GP.

LIST OF TABLES

Table1. Equivalent thermophysical properties, physical parameters and constants for 316L stainless steel.

Table 2. Processing parameters used in the L-DED experiment.

1. Introduction

1.1 Additive Manufacturing

Additive manufacturing is the process of creating an object by building it one layer at a time. It is the opposite of subtractive manufacturing, in which an object is created by cutting away at a solid block of material until the final product is complete.

Additive manufacturing, commonly known as 3D printing, is a transformative approach to industrial production that enables the creation of lighter, stronger parts and systems. It is the process of creating an object by adding material to it layer by layer, which is the opposite of subtractive manufacturing where material is removed from a solid block to create an object. This technology has evolved from prototyping in the 1980s to a production method that is now used to create functional products across various industries. Additive manufacturing works by first designing an object using computer-aided design (CAD) software or by scanning an existing object to create a digital blueprint. The design is then sliced into thin layers, which are built up one at a time by the 3D printer until the object is complete. This method allows for complex geometries and structures that would be difficult or impossible to achieve with traditional manufacturing methods. The currently available AM technologies allow complex end-usable parts to be manufactured and metal components. AM technologies divided into three main categories: i) powder bed systems ii) powder feed systems and iii) wire feed systems. The most common AM process for metal, in industrial applications are currently based on the powder bed process, in which a laser beam or an electron beam used to sinter or melt powder.

1.1.1 Benefits of Additive Manufacturing

- Enables the creation of complex geometries that are difficult or impossible with traditional manufacturing techniques.
- Allows for lightweight structures like lattice designs, reducing material usage and weight.
- Material is added only where needed, minimizing waste compared to subtractive methods like machining.
- Reduces the need for expensive tooling and molds, especially for low-volume production or prototypes.
- Speeds up product development cycles by enabling quick design iterations and testing.
- Ideal for producing one-off items or customized products, such as medical implants, dental devices, and bespoke consumer goods.
- Combines multiple parts into a single design, reducing assembly requirements and potential failure points.
- Reduces weight through topology optimization, crucial for aerospace, automotive, and robotics industries.
- Enables use of composite materials and functionally graded materials, improving product performance.
- New functions such as complex internal channels or several parts built in one.

1.2 Directed Energy Deposition Process

Directed Energy Deposition (DED) forms 3D objects by melting material as it is deposited using focused thermal energy, such as a laser, electron beam, or plasma arc. DED is one of the additive manufacturing processes, which uses 3D data to build objects layer by layer instead of using subtractive manufacturing technologies. The energy source and the material feed nozzle are manipulated using a gantry system or robotic arm. The centre of a typical DED system is the nozzle head, which consists of the energy source and the powder delivery nozzles. The nozzle head converges at the point of deposit where the laser beam is focused. The nozzle head is mounted on a multi-axis CNC head or an articulated arm. Typically, the build platform is part of the multi-axis CNC system, which includes the nozzle head. The following points describe the manufacturing of a product using DED.

1. The nozzle head and the build platform are moved using the geometric CAD information from the STL file of the object to create the geometry.
2. The laser beam melts the surface and creates a melt pool of the material on the substrate at the starting point along the build path.
3. The feeders feed the powder through the nozzle into the melt pool.
4. Using CAD geometric information, the controlled head or bed or both are moved along the build path to create the metal part feature.

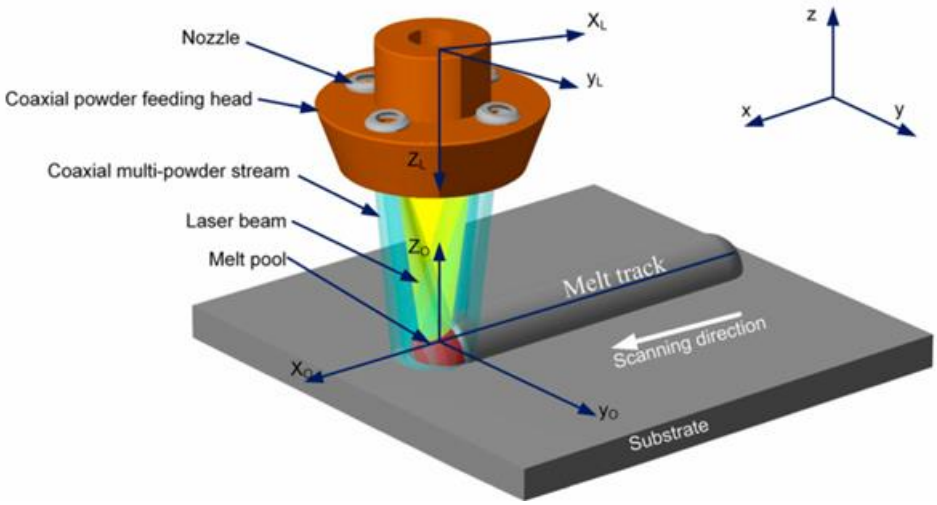

Fig1. Schematic of L-DED with multichannel coaxial powder feeding (C. Lei et al, 2024)

2. Problem Definition

The problem addressed in this paper is how the different special laser intensity profiles affect the shape and size of the melt pool during laser-based direct energy deposition(L-DED) process. Temperature distribution within the melt pool is also studied and how the velocity distribution within the melt pool is affected by the Marangoni stress.

A comparative analysis of the thermofluidic transport characteristics of L-DED is done under three different SLIPs including C-SGP, TE-GP and LE-GP. This can provide a theoretical foundation for improving the manufacturing properties. A three-dimensional numerical model is built using the COMSOL software for simulation of the thermofluidic transport coupling of the L-DED.

2.1 Model Configurations

A three-dimensional thermofluidic coupling model was used to do the numerical simulation. The dimensions of the model were taken as 14mm x 4mm x 3mm. The computational domain was partitioned into solid and liquid phase domains. The liquid phase domain dimensions were 14mm x 2mm x 1mm and other part is solid as shown in fig. A finer tetrahedral mesh was used

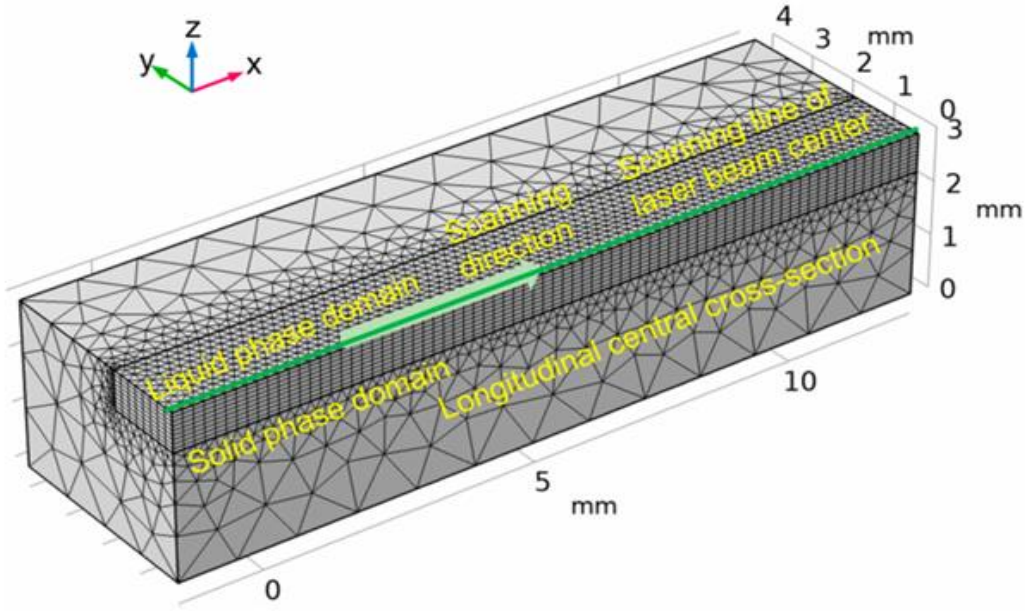

Fig. 2. Schematic of the simulated physical model and its computational mesh.

(C. Lei et al, 2024)

for liquid domain and a coarser tetrahedral mesh was used for solid domain for better accuracy, convergence and lower computational time. To optimise the simulation time, the simulated physical model was limited to half of the substrate and a single melt track along one side of the longitudinal central cross-section aligned with the laser beam scanning line.

3. Methodology

3.1. Basic Assumptions

(a) The Reynolds number and Mach number are significantly below their critical value so melt pool fluid flow can be assumed laminar and incompressible.

(b) Biot number for powder is far below 0.1 so it can be assumed that power melts instantaneously upon contacting the melt pool.

3.2. Governing Equation

Mass conservation equation

$$\nabla . \boldsymbol{u} = \mathbf{0} \qquad \textbf{(1)}$$

Where **u** is the melt flow velocity vector in Cartesian co-ordinate system.

Momentum conservation equation

$$\rho\frac{\partial(u)}{\partial t}+\ \rho(u.\nabla)u=-\nabla p+\mu\nabla^2u+\rho_{liq}g\alpha_{exp}\left(T-T_{liq}\right)-F_m \quad \textbf{(2)}$$

Where u refers to the melt flow velocity vector, t is time, μ is the dynamic viscosity, ρ_{liq} is the melt density, T and T_{liq} are separately transient temperature and liquidus temperature, p is static pressure, g stands for the acceleration of gravity α_{exp} refers to the thermal expansion coefficient, and F_m represents the resistance of dendrites in the mushy zone to fluid.

F_m depends on laser scanning velocity, melt velocity and volume fraction of the liquid phase[1].

Energy conservation equation

$$\rho\frac{\partial(h)}{\partial t}+\ \rho(u.\nabla h)=\nabla.(k\nabla T) \quad \textbf{(3)}$$

$$h=\ \int_{To}^{T}C_pdT\ +S_{liq}L \quad \textbf{(4)}$$

Where h is the enthalpy, k is the thermal conductivity, C_p is specific heat capacity and L is latent heat of fusion.

Laser Beam

The laser beam follows super Gaussian distribution, its special intensity profile is given by

$$I(x_L,y_L,z_L)=\frac{2^{\frac{1}{k}}KP}{\pi r_b^2\Gamma(\frac{1}{k})}\ \exp\left[-2\left(\frac{x_L^2+y_L^2}{r_b^2}\right)^k\right] \quad \textbf{(4)}$$

$$r_b=r_{0b}\sqrt{1+\left(\frac{z_d}{z_r}\right)^2} \quad \textbf{(5)}$$

Where k is super Gaussian order, p is laser power, r_b is equivalent beam radius, x_L,y_L,z_L are coordinates in laser coordinate system r_{0b} indicates the focus radius; z_d and z_r are the defocusing amount and Rayleigh range, respectively.

The elliptical Gaussian spatial profile of the laser beam can be expressed by

$$Q(x_L,y_L,z_L)=\frac{2P}{\pi r_{x_L}r_{y_L}}\ \exp\left[-2\left(\frac{x_L^2}{{r_{x_L}}^2}+\frac{y_L^2}{{r_{y_L}}^2}\right)\right]$$

Where r_{x_L} and r_{y_L} are the major and minor semiaxes of the elliptical Gaussian laser beam.

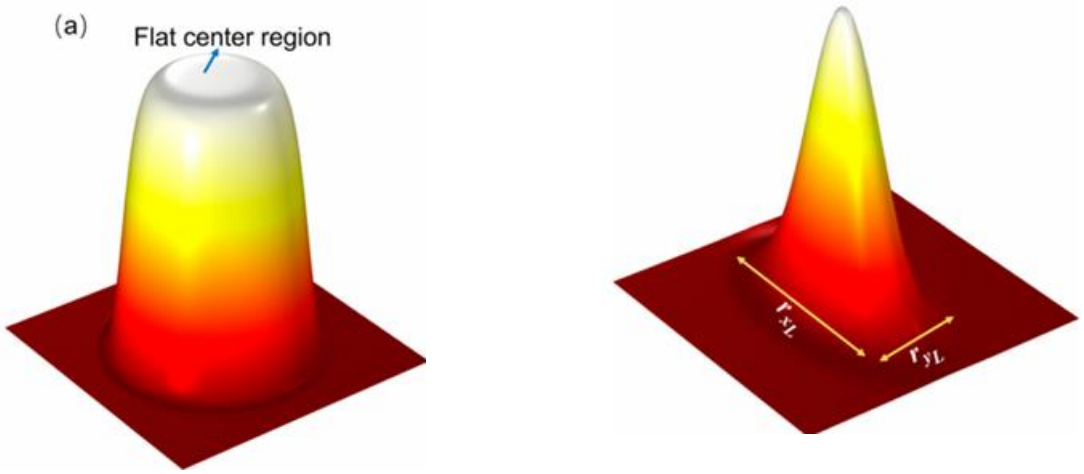

Fig3. (a) Circular super gaussian profile for k = 4.2. (b) Elliptic Gaussian intensity profile.

(C. Lei et al, 2024)

Coaxial Multi-powder Stream

The mass flux of powder is given by Gaussian distribution:

$$q_{CMS}(x_O, y_O, z_O) = \frac{2\dot{m}}{\pi R_{CMS}^2} \exp\left[-2\left(\frac{x_o^2+y_o^2}{R_{CMS}^2}\right)^2\right] \quad \textbf{(6)}$$

Where $\dot{m}$ is the powder feeding rate, R_{CMS} is the spot radius, x_o, y_o, z_o are coordinates of deposition system.

Marangoni Effect

The Marangoni effect is the mass transfer along an interface between two phases due to a gradient of the surface tension. The Marangoni number, a dimensionless value, can be used to characterize the relative effects of surface tension and viscous forces.

3.3. Boundary Conditions

The boundary condition at the interface is given by

$$Q_h(x,y) = \eta(1-\eta_{loss})I + I_{CMS} - \sigma\varepsilon\left(T^4 - T_\infty{}^4\right) - h_{con}(T-T_0) \quad \textbf{(8)}$$

Where Q_h is total heat flux at the melt pool surface, η is laser energy absorptivity, η_{loss} is laser attenuation rate, h_{con} is convective coefficient and I_{CMS} is the heat flux of the coaxial multi-powder stream [1].

The surface tenson force $F_{L/G}$ of melt pool is given by:

$$F_{L/G} = \sigma_T k.n_{L/G} - \Upsilon_T \nabla_s T \quad \textbf{(9)}$$

Where σ_T represents the surface tension coefficient, Υ_T is thermocapillary coefficient, k is the curvature of the melt pool surface and $n_{L/G}$ is the vector normal to the local free surface. The first term is normal surface tension, and second term is Marangoni shear stress.

3.4. Material Properties

Table 1 Equivalent thermophysical properties, physical parameters and constants for 316L stainless steel (C. Lei et al, 2024)

Parameters	**Values**
Solid specific heat C_{sol}	604 J·kg−1·K−1
Liquid specific heat C_{liq}	824 J·kg−1·K−1
Solid thermal conductivity k_{sol}	25 W·m−1·K−1
Liquid thermal conductivity k_{liq}	36 W·m−1·K−1
Solid density ρ_{sol}	8000 kg·m−3
Liquid density ρ_{liq}	6893 kg·m−3
Solid/liquid emissivity ε	0.7 %
Solid liquid absorptivity η	0.37 %
Solidus temperature T_{sol}	1648 k
Liquidus temperature T_{liq}	1673 k
Latent heat of fusion L	2.5×10^5 J·kg−1
Convective heat transfer coefficient h_{con}	80 $W.m^{-2}.k^{-1}$
Dynamic viscosity μ	$6 \times 10^{-3}\ kg.m^{-1}.s^{-1}$
Stefan- Boltzmann constant, σ	5.67×10^{-8} W.$m^{-2}.k^{-4}$
Thermal expansion coefficient α_{exp}	5.85×10^{-5} k^{-1}

4. Experimental Analysis

4.1 Numerical Simulation

COMSOL software is used to solve the coupled mass, energy and momentum equations. Mass, momentum and energy conservation equations was solved to find temperature and velocity fields of the melt pool.

5. Results and Discussion

5.1. Experiment Results

The experimental vs simulated cross section profile of the melt pool is shown in fig8. The two are compared for different laser powers using circular super-Gaussian profile(C-SGP). It can be observed that the predicted and experimental cross-section exhibit the same saucer shaped profile. As shown in fig9 the hight, width and depth of the melt pool increases with increase in laser power. Due to high laser power, the heat input and laser intensity on melt pool increases which leads to a longer, wider and deeper melt pool. The error between the experimental and simulation results is very small so it will be reasonable to use this model to study the melt pool under different SLIPs.

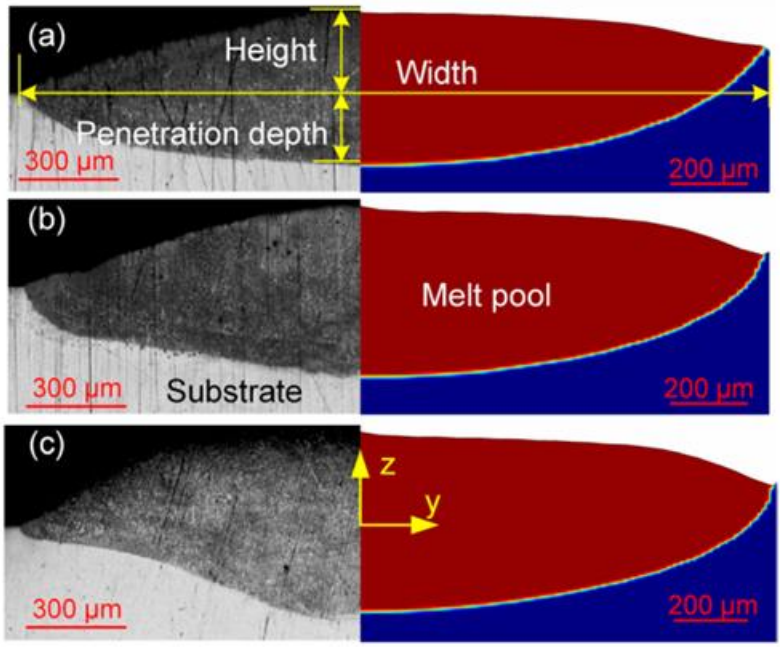

Fig.4. Cross-sectional profiles of the melt pool under the C-SGP with different laser powers: (a) 600 W, (b) 700 W, and (c) 800 W. (C. Lei et al, 2024)

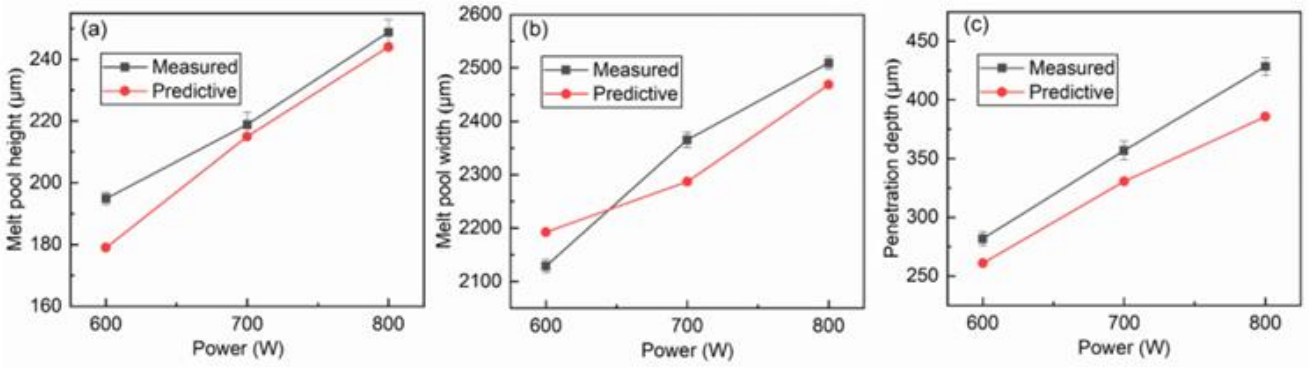

Fig. 5. Measured and predicted melt pool sizes: (a) height; (b) width; (c) penetration depth. (C. Lei et al, 2024)

Table 2. Processing parameters used in the L-DED experiment (C. Lei et al, 2024)

Processing parameters	value
Laser power P	600, 700, 800 W
Laser scanning speed V	600 $mm.min^{-1}$
Powder feeding rate $\dot{m}$	10.2 $g.min^{-1}$
Spot radius of coaxial multi powder stream R_{CMS}	2 mm
Laser spot radius r_b	1.2 mm
Laser defocusing amount z_d	11 mm

5.2. Simulation Results

The simulations were done for different special laser intensity profiles (i.e. C-SGP, TE-GP and LE-SGP). As shown in fig10 the melt pool geometries are like the corresponding to the laser spots of the three SLIPs. The size of the melt pool is slightly larger than the laser spots because of the conduction and convection of heat from the laser spot to the outward direction towards the solid region.

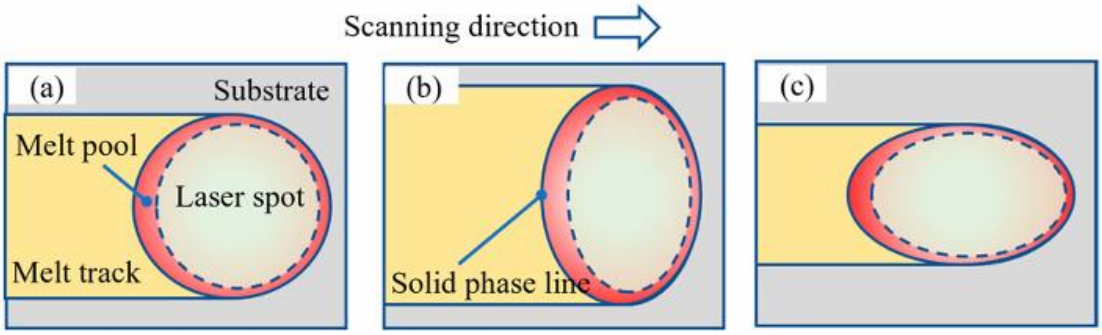

Fig.6. Schematics of melt pool geometries under three SLIPs: (a) C-SGP, (b) TE-GP, and (c) LE-GP. (C, Lei et al, 2024)

From fig it can be observed that the peak temperatures under C-SGP, TE-GP and LE-GP are 2414 K, 2562 K and 2863 K, respectively. The peak temperature under C-SGP is lowest due to its lowest peak intensity. The peak temperature of LE-GP is higher than TE-GP because of its major axis align with the scanning direction resulting in extended duration of heating of the melt pool.

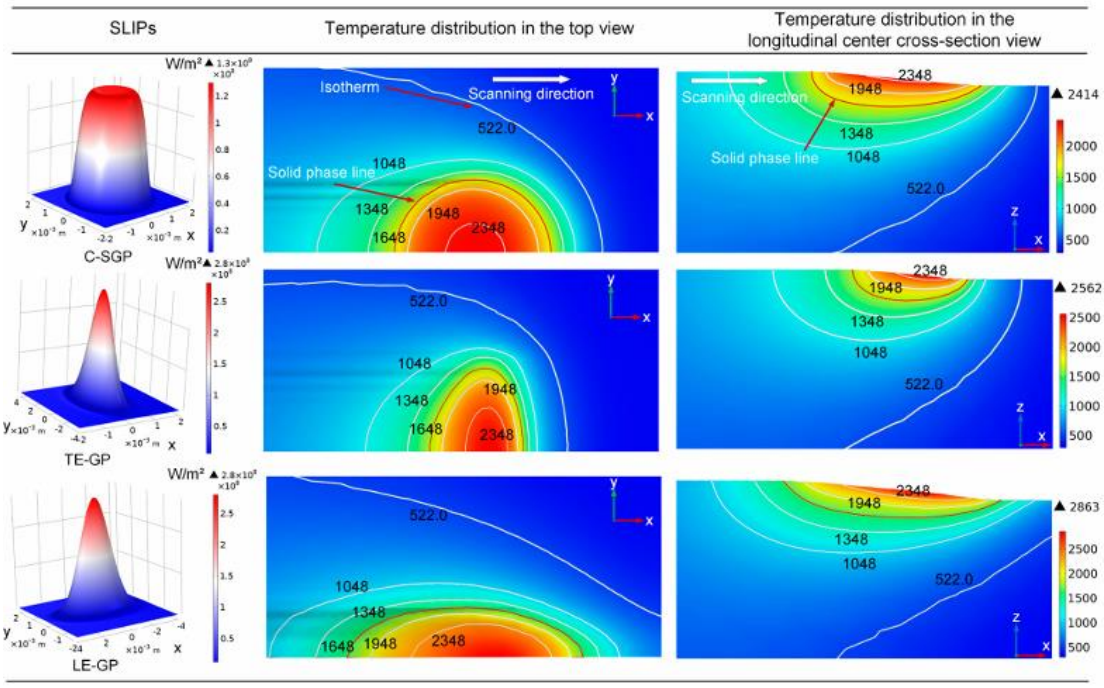

Fig.7. Temperature fields under the three SLIPs.
(C, Lei et al, 2024)

5.3. Velocity Distribution

Fig.11 shows velocity profiles of the melt pool for three SLIPs. The Marangoni number for the three SLIPs is much greater than 1 so the flow field is governed by the Marangoni effect. As shown in fig the upper surface fluid flow away from the central region towards the melt pool boundary and for a momentum balance lower layer fluid flow towards the centre thereby

forming a outward flow vortex. From the fig it can be seen that fluid has maximum velocity under LE-GP followed by TE-GP and C-GP.

When the temperature of the melt pool exceeds the critical temperature of thermocapillary coefficient, the thermocapillary coefficient becomes negative thereby the Marangoni shear stress becomes in the direction of heat flow. Therefore, the fluid at the surface starts flowing towards edges.

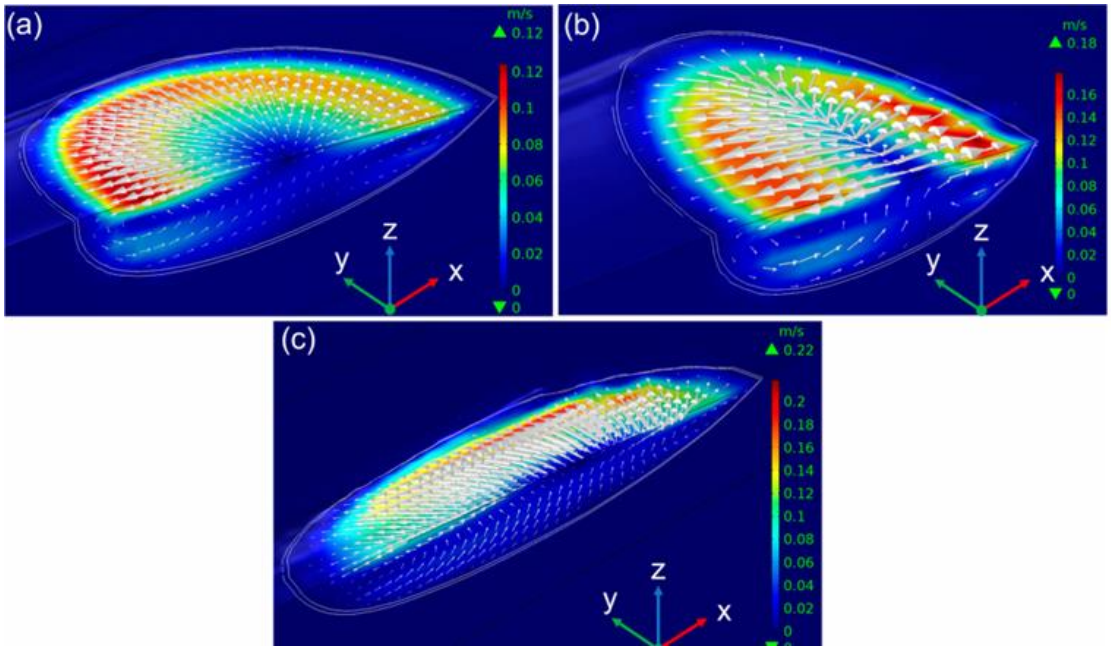

Fig.8. Velocity fields of the melt pool under three SLIPs: (a) C-SGP, (b) TE-GP, and (c) LE-GP. (C. Lei et at, 2024)

6. Conclusions

1) The geometries of the melt pool under the three SLIPs are somewhat similar to their corresponding SLIP geometry. The aspect ratio of melt pool is maximum for the LE-GP while it is minimum for the TE-GP. The curvature of the solidification interface fabricated using the LE-GP is found to be the smallest compared to that fabricated using the C-SGP and TE-GP, which exhibit comparable curvatures.
2) All three SLIPs exhibit a circular vortex pattern and fluid flows outwards in the melt pool. The peak fluid velocity is larger in LE-GP than TE-GP and C-SGP. The Marangoni convection effect dominates the fluid flow in all three SLIPs, but it is strongest in the LE-GP and weakest in the TE-GP.
3) The heat transport processes within the melt pool under both C-SGP and TE-GP are jointly dominated by heat convection and conduction, while those under the LE GP are dominated by heat convection. The average temperature gradient is higher under TE-GP than C-SGP and LE-GP, which leads to columnar grain formation.

7. Scope for Future Work

In this paper, we see that the melt pool shape and size has greatly affected by laser special variation. In future we can make variations in other parameters to observe the dependency of melt pool dynamics and its solidification.

8. References

1. Chao jiao Lei, Song Ren, Cunhong Yin, Xixia Liu, Mingfei Chen, Jiazhu Wu & Changjun Han (2024) Manipulating melt pool thermofluidic transport in directed energy deposition driven by a laser intensity spatial shaping strategy, Virtual and Physical Prototyping, 19:1, e2308513.

2. Gabriele Piscopo, Eleonora Atzeni, Abdollah Saboori and Alessandro Salmi (2022). An Overview of Physical Phenomena Involved in the Laser Powder Directed Energy Deposition Process.

3. Mohammadreza Lalegani Dezakia, Ahmad Serjoueia, Ali Zolfagharianb, Mohammad Fotouhic, Mahmoud Moradid, M.K.A. Ariffine, Mahdi Bodaghi (2022) A review on additive/subtractive hybrid manufacturing of directed energy deposition (DED) process.